inorganics

MDPI

Article

Insights into Pd-Nb@In_2Se_3 Electrocatalyst for High-Performance and Selective CO_2 Reduction Reaction from DFT

Lin Ju [1,*], Xiao Tang [2], Yixin Zhang [1], Mengya Chen [1], Shuli Liu [1] and Chen Long [1]

[1] School of Physics and Electric Engineering, Anyang Normal University, Anyang 455000, China; 221101089@stu.aynu.edu.cn (Y.Z.); ciky-825@stu.aynu.edu.cn (M.C.); 01958@aynu.edu.cn (S.L.); longchen@aynu.edu.cn (C.L.)
[2] College of Science, Nanjing Forestry University, Nanjing 210037, China; xiaotang@njfu.edu.cn
* Correspondence: julin@aynu.edu.cn

Abstract: The electrochemical CO_2 reduction reaction (eCO_2RR), driven by renewable energy, represents a promising strategy for mitigating atmospheric CO_2 levels while generating valuable fuels and chemicals. Its practical implementation hinges on the development of highly efficient electrocatalysts. In this study, a novel dual-metal atomic catalyst (DAC), composed of niobium and palladium single atoms anchored on a ferroelectric α-In_2Se_3 monolayer (Nb-Pd@In_2Se_3), is proposed based on density functional theory (DFT) calculations. The investigation encompassed analyses of structural and electronic characteristics, CO_2 adsorption configurations, transition-state energetics, and Gibbs free energy changes during the eCO_2RR process, elucidating a synergistic catalytic mechanism. The Nb-Pd@In_2Se_3 DAC system demonstrates enhanced CO_2 activation compared to single-atom counterparts, which is attributed to the complementary roles of Nb and Pd sites. Specifically, Nb atoms primarily drive carbon reduction, while neighboring Pd atoms facilitate oxygen species removal through proton-coupled electron transfer. This dual-site interaction lowers the overall reaction barrier, promoting efficient CO_2 conversion. Notably, the polarization switching of the In_2Se_3 substrate dynamically modulates energy barriers and reaction pathways, thereby influencing product selectivity. Our work provides theoretical guidance for designing ferroelectric-supported DACs for the eCO_2RR.

Keywords: electrochemical CO_2 reduction reaction; density functional theory; dual-metal atomic catalyst; ferroelectric

check for updates

Academic Editor: Axel Klein

Received: 10 April 2025
Revised: 1 May 2025
Accepted: 3 May 2025
Published: 5 May 2025

Citation: Ju, L.; Tang, X.; Zhang, Y.; Chen, M.; Liu, S.; Long, C. Insights into Pd-Nb@In_2Se_3 Electrocatalyst for High-Performance and Selective CO_2 Reduction Reaction from DFT. *Inorganics* **2025**, *13*, 146. https://doi.org/10.3390/inorganics13050146

Copyright: © 2025 by the authors. Licensee MDPI, Basel, Switzerland. This article is an open access article distributed under the terms and conditions of the Creative Commons Attribution (CC BY) license (https://creativecommons.org/licenses/by/4.0/).

1. Introduction

Carbon dioxide (CO_2), a principal climate-altering gas, drives critical environmental challenges including rising global temperatures, climatic instability, ocean acidification, and ecological carbon cycle disturbances [1,2]. Urgent action is required to achieve net-zero anthropogenic carbon dioxide equivalent emissions by 2050, as mandated by the Intergovernmental Panel on Climate Change (IPCC) to cap global temperature increases at 1.5 °C above preindustrial baselines [3]. This imperative is becoming increasingly critical given the persistent reliance on emission-generating technologies and escalating global energy demands. Addressing the dual challenge of atmospheric CO_2 mitigation and sustainable utilization has emerged as a pivotal research frontier [4–7]. Carbon management encompasses three interconnected approaches to mitigating anthropogenic CO_2 emissions. First, energy generation processes are being optimized through advanced combustion

technologies, such as oxy-fuel combustion with pure oxygen injection and homogeneous charge compression ignition (HCCI) engines using biofuel blends [8,9]. Second, modern carbon capture technologies are advancing beyond conventional geological storage in saline aquifers or depleted oil fields by transforming captured CO_2 into value-added products like construction aggregates, agricultural bio-fertilizers, and energy-efficient syngas, leveraging advanced separation processes such as pressure swing adsorption (PSA) and membrane systems [10,11]. Third, the chemical conversion pathways, particularly electrocatalytic CO_2 reduction reaction (eCO_2RR), utilize multi-electron transfer processes ($2e^-$ to $12e^-$) with tailored catalysts (e.g., Cu for hydrocarbons, Ag/Zn for CO) to produce value-added fuels and chemicals like CO, formate, methane, ethylene, and ethanol, while enabling renewable energy integration and high-pressure reactor designs for industrial scalability [12,13].

Among the above approaches, the eCO_2RR stands out for its dual capacity to mitigate emissions and generate valuable chemical feedstocks [14–16]. And this technology has four key advantages. First, the eCO_2RR leverages renewable electricity from solar, wind, or tidal energy to convert CO_2 into chemicals, enabling carbon-neutral cycles while reducing reliance on fossil fuels [17]. Second, the process generates high-value chemicals like ethylene (feedstock for plastics) [18], methane (fuel) [19], and formate (industrial reagent) [20], directly replacing fossil-derived equivalents in existing supply chains. Third, unlike thermocatalytic methods requiring high temperatures/pressures, the eCO_2RR operates efficiently at room temperature and atmospheric pressure, reducing energy demands and infrastructure complexity. Forth, modular flow cell designs and membrane electrode assemblies (MEAs) allow scalable deployment for industrial adoption [21].

The eCO_2RR process involves intricate multi-stage reaction sequences: (1) CO_2 adsorption at electrode interfaces; (2) proton=coupled electron transfer (PCET) steps, which forms C–H bonds with broken C=O bonds; and (3) detachment of synthesized compounds from active sites through desorption mechanisms and their subsequent transport into the bulk reaction medium via dissolution–diffusion pathways [22]. This sequential process becomes particularly consequential in water-containing systems where the parasitic hydrogen evolution reaction (HER) actively competes with the CO_2RR for catalytic resources and electron transfer, fundamentally altering the thermodynamic landscape and resulting in suboptimal product distributions [23].

In the process of reducing CO_2 with metal electrodes, there are many challenges, including the impact of the poor stability of the electrodes. Many metal electrodes, such as palladium (Pd), indium (In), and tin (Sn), have stability issues when reducing CO_2. Take Pd as an example; CO has strong adsorption energy on its surface, which causes the electrode to be easily poisoned and deactivated, greatly shortening its service life [24]. Although In and Sn electrodes can achieve the reduction of CO_2, they often require a higher voltage to drive the reaction [25–27], which not only causes a large waste of energy but may also trigger side reactions due to high voltage, further reducing the selectivity and efficiency of the reaction. At the same time, the stability of the electrode deteriorates further under high voltage, accelerating the electrode's wear and tear. These problems seriously restrict the practical application of metal electrodes in the field of CO_2 reduction [26]. Effective eCO_2RR implementation hinges on catalytic systems being optimized across three critical dimensions, namely conversion efficiency under applied potentials, target product selectivity over competing reactions, and long-term structural and functional stability. These properties are intrinsically linked to atomic-scale catalyst architecture, particularly the coordination environment of active sites.

Since the conceptualization of single-atom catalysts (SACs) in 2011, these atomically dispersed metal systems have revolutionized catalytic research through maximum metal utilization efficiency (approaching 100%) [28–33], well-defined active site geometries for

mechanistic studies [34–36], and enhanced selectivity profiles compared to nanoparticle analogues. However, SAC implementation faces two fundamental constraints: low active site density due to synthesis limitations and inadequate multi-intermediate stabilization in complex eCO_2RR pathways [37,38]. This has prompted researchers to turn their attention to bimetallic atomic catalyst (DAC) systems with greater structural flexibility.

DACs exhibit distinct advantages over isolated SACs, combining the inherent merits of SACs with supplementary synergistic benefits: (1) DACs substantially elevate metal loading capacities while expanding the population of accessible reactive centers, a critical factor for scalable catalytic applications [39]; (2) DACs permit dynamic spatial arrangements of active sites, enabling coordinated interactions essential for multi-step CO_2 reduction pathways [40,41]; (3) electronic modulation between dissimilar metal atoms allows precise regulation of intermediate binding strengths, creating tunable platforms for reaction pathway optimization and selectivity control [40,42–47]; (4) independent yet coexisting metallic centers enable parallel reaction channels, permitting simultaneous production of distinct value-added compounds through site-specific catalytic processes [48]; (5) and in DACs, one metallic component can modify support interactions that subsequently influence the catalytic behavior of adjacent metal sites, creating cascading activation mechanisms [30,49,50]. It is anticipated that further studies will concentrate on enhancing the performance of bimetallic atomic site catalysts.

Contemporary DACs predominantly utilize two-dimensional nitrogen-doped carbon substrates, as exemplified by Fe-Co [51], Ni-Fe [52], and Co-Pt [53] dual-atom configurations, which have been fabricated with dual-solvent, pyrolysis, and cyclic voltammetry methods, respectively. However, these conventional DACs exhibit inherent limitations in post-synthesis catalytic tunability due to their inability to leverage substrate property modifications for performance enhancement. Recent advancements in ferroelectric material engineering provide a promising solution. Substantial theoretical and experimental evidence demonstrates that polarization direction modulation in ferroelectrics not only governs molecular adsorption/desorption dynamics but also enables precise control over surface catalytic activity and product selectivity [54–56]. Capitalizing on this principle, we engineered a novel ferroelectric DAC system by anchoring niobium (Nb) and palladium (Pd) single atoms onto an α-In_2Se_3 monolayer substrate (Nb-Pd@In_2Se_3). The α-In_2Se_3 monolayer is a van der Waals material exhibiting coupled in-plane and out-of-plane ferroelectric polarization at room temperature [56–58]. It features a quintuple atomic-layer structure (Se-In-Se-In-Se) with spontaneous polarization arising from asymmetric Se atom displacements, enabling bidirectional electric field control of both polarization axes. This unique architecture allows for the dynamic regulation of metal–support interactions, addressing the static catalytic behavior inherent to traditional carbon-based DACs. The theoretical analysis revealed that the dual-metal atomic configuration significantly enhances CO_2 activation capability during the eCO_2RR process. In the synergistic catalytic mechanism, the Nb atomic sites predominantly function as catalytic centers for carbon reduction, while the adjacent Pd counterparts facilitate oxygen species removal through a complementary catalytic pathway. Notably, polarization switching of the ferroelectric substrate modulates both the energy barriers along the reaction coordinates and the dominant reaction pathways, ultimately dictating the selectivity of terminal products.

2. Results and Discussion

2.1. Geometric Structures of Nb-Pd@In_2Se_3

The 2D ferroelectric α-phase In_2Se_3 monolayer was chosen as the substrate material. Based on our previous work [56], we selected Pd and Nb transition metals as candidates for loaded metallic dual atoms, since they can stably form Pd@In_2Se_3 and Nb@In_2Se_3

SACs. According to the position of the intermediate Se layer offset (see Figure 1a,b), the α-In_2Se_3 monolayer has two stable polarization phases, namely polarization upward (P↑) and downward (P↓). We refer to the configuration where the Pd-Nb dual-atom pair is doped on the outer surface of two layers with a Se spacing of 3.06 Å as the Pd-Nb@P↓-In_2Se_3. Moreover, the configuration where the Pd-Nb dual-atom pair is doped on the outer surface of two layers of Se with a spacing of 3.84 Å is called Pd-Nb@P↑-In_2Se_3. As for the SACs [59–61], strong binding strength is essential for the stability of DACs. At the energetically most favorable site, the binding energy of the Nb-Pd dual-atom pair in Pd-Nb@P↓-In_2Se_3 and Pd-Nb@P↑-In_2Se_3 were −15.69 and −12.27 eV/unit, respectively. The low binding energies indicate that there is a strong interaction between the metal atoms and the substrate, as evidenced by the strong covalent Pd–Se and Nb-Se bonds (see Figure 1a,b), which are caused by the strong hybridization of Se *p* and Pd/Nb *d* orbitals near the Fermi level (see Figure S1a,b).

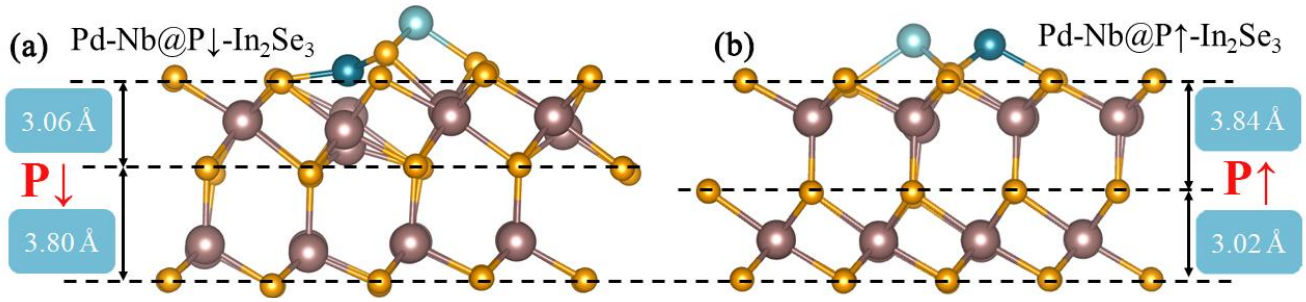

Figure 1. Side views of the optimized configuration of (**a**) Pd-Nb@P↓-In_2Se_3 and (**b**) Pd-Nb@P↑-In_2Se_3 DACs.

To further demonstrate the structural stability of Pd-Nb@In_2Se_3, ab initio molecular dynamics (AIMD) calculations were carried out on these two configuration at a temperature of 1000 K, with a time step of 1 fs and a total time length of 10 ps (see Figure 2a,b). During the AIMD simulations, the geometrical structure did not change significantly, and the total energy of the system tended to be stable, indicating that these configurations have good thermal stability. Overall, both the binding energy and molecular dynamics simulation results show the promising feasibility of fabricating Pd-Nb@In_2Se_3 DACs.

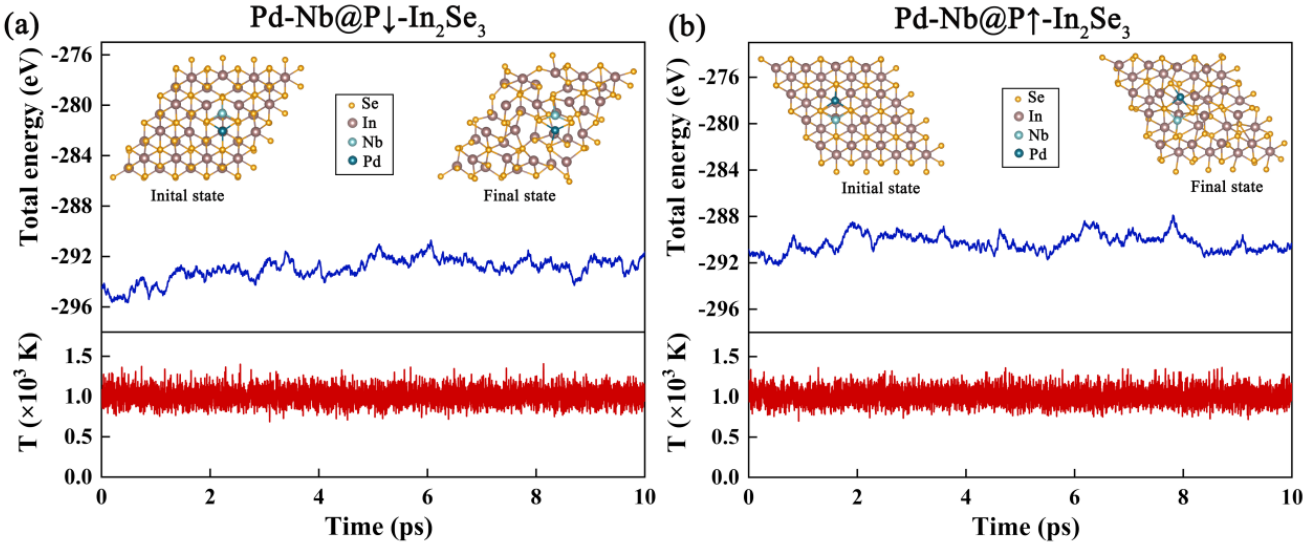

Figure 2. The ab initio molecular dynamics simulations of (**a**) Pd-Nb@P↓-In_2Se_3 and (**b**) Pd-Nb@P↑-In_2Se_3 configurations at 1000 K, showing the fluctuations in the total energy (upper) and temperature (lower) over a time step of 1 fs and a duration of 10 ps.

2.2. Activation of CO_2 on Pd-Nb@In_2Se_3 DACs

The effective activation of CO_2 molecules is a key step for the subsequent reduction reaction. The linear structure of CO_2 molecules contributes to their pronounced chemical inertness, primarily due to the symmetry-induced cancellation of dipole moments despite the presence of polar C=O bonds. This linear geometry stabilizes the molecule thermodynamically, as the two C=O bonds exhibit dissociation energies of approximately 750 kJ·mol^{-1}. Additionally, the large energy gap (13.7 eV) between the highest occupied molecular orbital (HOMO) and lowest unoccupied molecular orbital (LUMO) creates a significant kinetic barrier to electron transfer, necessitating substantial energy input for chemical transformations. In catalytic systems employing isolated atomic site catalysts (SACs), CO_2 adsorption typically occurs via either oxygen– or carbon–metal (O-M or C-M) interactions at the active metal centers. However, the limited electron donating capacity and geometric constraints of isolated atomic sites restrict the extent of CO_2 activation. Consequently, SACs often require elevated temperatures and pressures to achieve moderate reaction rates, further reducing reaction efficiency and selectivity toward multi-carbon products.

Dual-site catalysts can demonstrate enhanced CO_2 adsorption via coordination involving both metallic dual atoms and support atoms, requiring lower activation energy than the SAC to activate CO_2 [62]. As shown in Table S1, by separately comparing the adsorption energy of CO_2 on the Pd and Nb sites of Pd-Nb@In_2Se_3 DACs (see Figure S2), we conclude that the adsorption of CO_2 on the Pd site had more negative adsorption energy in both P↑ and P↓ configurations, which means the CO_2 tends to adsorb on the Pd site of Pd-Nb@In_2Se_3 DACs. The ∠OCO values of CO_2 adsorbed on Pd-Nb@P↓-In_2Se_3 and Pd-Nb@P↑-In_2Se_3 were significantly reduced to 131.38° and 125.18° from an initial value of 180°, respectively. Based on the structural analysis, it could be stated that the Pd-Nb@In_2Se_3 catalyst could effectively activate CO_2 molecules. Moreover, according to our previous report [56] that the ∠OCO values of CO_2 adsorbed on Pd@P↓-In_2Se_3 and Pd@P↑-In_2Se_3 were 149.2° and 151.2°, respectively, it can be concluded that the synergistic effect of a bimetallic atomic site causes a more obvious deformation of adsorbed CO_2 molecules (17.82° and 26.02° for P↓ and P↑, respectively), indicating a higher activation of CO_2. The similar synergistic effects in the Pt-Ni@CeO_2 bimetallic system were extensively validated through comprehensive characterization and computational studies [62]. Temperature-programmed reduction (TPR) and desorption (TPD) analyses revealed that Pt-Ni synergy significantly enhances the generation of reactive oxygen intermediates (e.g., surface peroxides and hydroxyl radicals) and strengthens metal–support interactions via charge transfer mechanisms. These modifications collectively optimize CO_2 chemisorption capacity, as evidenced by the higher adsorption efficiency compared to the monometallic counterparts (Pt@CeO_2 and Ni@CeO_2). Density functional theory (DFT) simulations further demonstrated a 35–40% reduction in CO_2 activation energy (E_a = 10.1 kcal mol^{-1} for Pt-Ni@CeO_2 vs. 32.9 and 36.5 kcal mol^{-1} for Ni@CeO_2 and Pt@CeO_2, respectively), which is attributed to electronic structure modulation at Pt-Ni-CeO_2 interfacial sites.

In order to explore the activation mechanism, we employed a charge density difference calculation, which demonstrated that there is both a loss and gain of electrons on the adsorbed CO_2 molecule and the bimetallic atomic sites (see Figure 3a,b). This is because the empty Pd/Nb *d* orbital can accept electrons from the highest occupied molecular orbitals ($1\pi_g$ orbital) of the CO_2 molecule, while the occupied Pd/Nb *d* orbital can back-donate electrons to the lowest unoccupied molecular orbitals ($2\pi_u$ orbital) of the CO_2 molecule (see Figure 3c). The synergy of electron donation and backdonation-dependent *d* orbital occupation ensures that CO_2 can be efficiently activated [56].

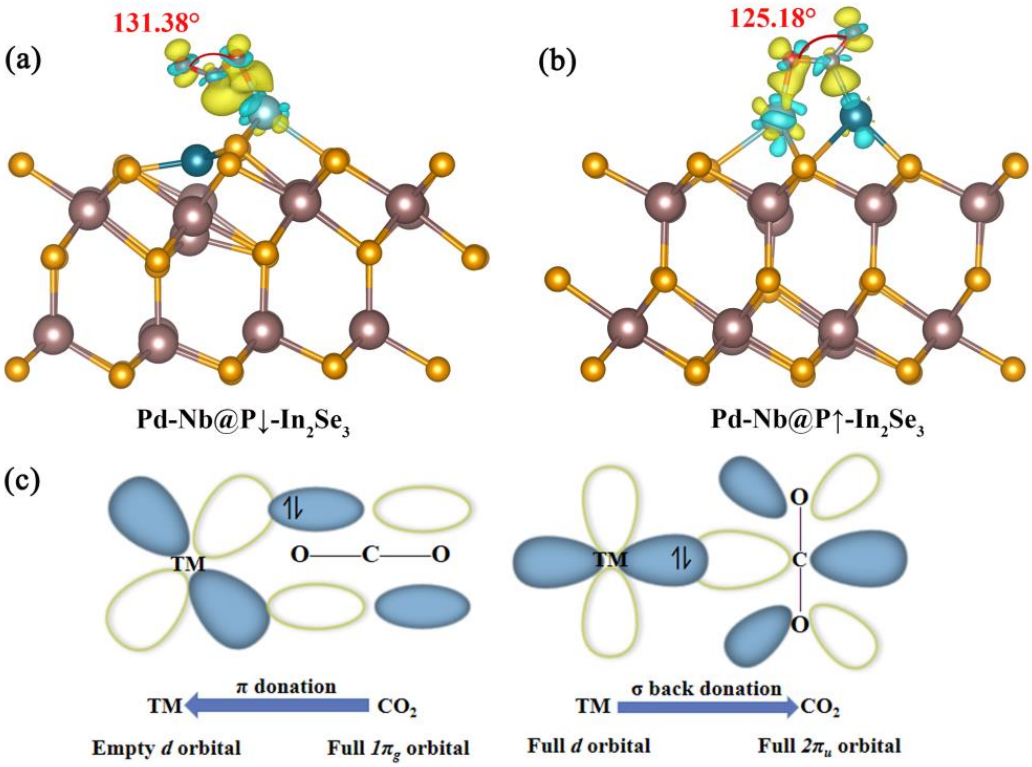

Figure 3. The charge differential density plots of CO_2 adsorbed on (**a**) Pd-Nb@P↓-In_2Se_3 and (**b**) Pd-Nb@P↑-In_2Se. The charge accumulation is indicated by areas that are yellow. The charge depletion is indicated by areas that are cyan. The value of the isosurface is 0.01 e $Å^{-3}$. (**c**) Simplified schematic diagrams of CO_2 activation on transition metals.

As mentioned before, the CO_2 adsorbed on Pd-Nb@P↑-In_2Se_3 (∠OCO = 125.18°) had a more obvious deformation than that absorbed on Pd-Nb@P↓-In_2Se_3 (∠OCO = 131.38°), which means Pd-Nb@P↑-In_2Se_3 has higher CO_2 activation. In order to investigate the reason for this, we calculated the Pd and Nb *d* orbitals in Pd-Nb@P↑-In_2Se_3 and Pd-Nb@P↓-In_2Se_3 DACs, respectively. Then, based on the partial electronic orbitals (see Figure 4a), we obtained the *d* band center of the Pd and Nb atoms for both kinds of Pd-Nb@In_2Se_3 DACs. As displayed in Figure 4b, both *d* band centers of the Pd (−2.09 eV) and Nb (0.11 eV) atoms in Pd-Nb@P↑-In_2Se_3 were closer to the Fermi level than the ones of Pd (−2.68 eV) and Nb (0.44 eV) atoms in Pd-Nb@P↓-In_2Se_3. And it has been reported that the exceptional electrocatalytic performance of Co_2 anchored graphdiyne in nitrogen fixation originates from the presence of localized electronic states adjacent to the Fermi level, which optimize charge transfer dynamics during the reaction [63]. Therefore, in the case of P↑, the proximity of the *d* band center of Pd and Nb atoms to the Fermi level induces a high CO_2 activation performance. Note that the different *d* band centers of bimetallic atomic sites in Pd-Nb@In_2Se_3 under different polarization states implies that both the reaction path and the limiting potential of the subsequent CO_2 hydrogenation process may be affected by the polarization switch.

2.3. eCO₂RR on Pd-Nb@In₂Se₃ DACs

Considering the complexity of the CO_2 reaction (see Figure S3), we have summarized the minimum-energy reaction paths of the CO_2RR over Pd-Nb@In_2Se_3 catalysts (see Figure 5). The CO_2RR pathways over Pd-Nb@In_2Se_3 catalysts exhibit stark polarization-dependent selectivity, governed by the structural and electronic asymmetry induced by the ferroelectric In_2Se_3 substrate's polarization orientation (P↓ and P↑). The CO_2 reduction reaction begins with the adsorption of CO_2 onto the Pd-Nb@P↓-In_2Se_3 catalyst surface,

forming a CO_2 intermediate ($CO_2 + * \rightarrow CO_2*$). This adsorbed CO_2 undergoes a proton-coupled electron transfer (PCET) step, where one hydrogen atom binds to an O atom ($CO_2* + H^+ + e^- \rightarrow OCHO*$), leading to the formation of an OCHO intermediate (bent configuration with O–CH–O bonding). Subsequently, a second protonation occurs at the adjacent oxygen atom ($OCHO* + H^+ + e^- \rightarrow HOCHO*$), stabilizing the HOCHO intermediate (adsorbed formate-like structure). Finally, the HOCHO intermediate desorbs from the catalyst surface ($HOCHO* \rightarrow HOCHO + *$), releasing formic acid (HOCHO) as the end product. Due to the high energy barrier associated with stabilizing the second protonation step, the rate-determining step (PDS) is identified as the transformation of $OCHO* \rightarrow HOCHO*$, requiring an applied potential of −0.45 V vs. RHE. In contrast, in the CO_2RR on a Pd-Nb@P↑-In_2Se_3 catalyst, the reaction course is significantly different from that on Pd-Nb@P↓-In_2Se_3, which undergoes an alternative protonation pathway. The first PCET step preferentially protonates the carbon atom, forming the OCOH intermediate ($CO_2* + H^+ + e^- \rightarrow OCOH*$) (linear configuration with O–C–O–H bonding). Further reduction cleaves the C–O bond. A second protonation occurs at the hydroxyl group of OCOH intermediate. The hydroxyl group binds a hydrogen ion to generate H_2O and desorb ($OCOH* + H^+ + e^- \rightarrow CO* + H_2O$), producing a CO intermediate adsorbed on the Pd site of the catalyst. Sequential hydrogenation steps follow: $CO* + H^+ + e^- \rightarrow CHO*$ (formyl), $CHO* + H^+ + e^- \rightarrow CH_2O*$ (formaldehyde-like) and $CH_2O* + H^+ + e^- \rightarrow CH_{2*} + OH*$ via C–O bond scission. The critical C–O bond scission step ($CH_2O* + H^+ + e^- \rightarrow CH_2* + OH*$) in the methane production pathway over the Pd-Nb@P↓-In_2Se_3 catalyst is driven by the synergistic interplay between the Pd and Nb dual active sites. The CH_2 intermediate absorbs the Pd site, and the OH intermediate absorbs the Nb site. CH_2* undergoes progressive hydrogenation ($CH_2* + OH* + H^+ + e^- \rightarrow CH_3* + OH*$), followed by a critical step where CH_3 reacts with a co-adsorbed OH group to form CH_3 and H_2O ($CH_3* + OH* + H^+ + e^- \rightarrow CH_3* + H_2O*$). Then, the H_2O molecule desorbs from the Nb site ($CH_3* + H_2O* \rightarrow CH_3* + H_2O$). This step is identified as the PDS, with a limiting potential of −0.66 V vs. RHE, reflecting the substantial energy required for H_2O dissociation. The final hydrogenation of CH_3 yields methane (CH_4) ($CH_3* + H^+ + e^- \rightarrow CH_4*$), which desorbs from the catalyst surface ($CH_4* \rightarrow CH_4 + *$). Consequently, the U_l, catalytic pathway, and the ultimate products during the eCO_2RR, are governed by polarization orientation and are adjustable via ferroelectric switching. Moreover, compared to the U_l of Pd@In_2Se_3 SACs for the eCO_2RR (−0.77 V under the P↓ state and −0.87 V under the P↑ state) [56], each corresponding Pd-Nb@In_2Se_3 DAC for the eCO_2RR has a smaller U_l, indicating that the synergistic effect of the bimetallic atomic site could effectively lower the eCO_2RR barrier. According to the reduction reaction path of $CH_2O* \rightarrow CH_2* + OH* \rightarrow CH_3* + OH* \rightarrow CH_3*$, we found that carbon-containing intermediates (e.g., CH*, CH_2*) tend to undergo hydrogenation reduction at Pd atomic sites, while oxygen-containing intermediates (e.g., OH*) prefer to be hydrogenated and reduced into water at Nb atomic sites (see Figure S4). Therefore, the synergistic effect of Nb-Pd dual-site metal atoms can be described as such: Pd sites act as functional sites for carbon reduction, whereas Nb sites serve as functional sites for oxygen removal. Notably, the U_l of Pd@In_2Se_3 SACs for the eCO_2RR (−0.45 V under the P↓ state and −0.66 V under the P↑ state) are markedly superior to those of conventional eCO_2RR catalysts, such as Cu (211) (−0.8 V) [64], Co@Cu (−0.87 V) [65], and WC (0001) (−1.0 V) [66]. Since the equilibrium potential (E°) for the formation of HCOOH and CH_4 from CO_2, respectively, are −0.25 V vs. RHE and 0.17 V vs. RHE at pH = 0 [67], the corresponding overpotentials are −0.2 V vs. RHE and −0.83 V vs. RHE, which are lower than the ones of many eCO_2RR electrocatalysts synthesized experimentally, such as Pd_2 (−0.85 V vs. RHE for generating CO) [68], NiCu-NC (−1.07 V vs. RHE for generating CO) [69], FeNi-NSC (−1.0 V vs. RHE for generating CO) [70],

Cu/Ni-NC (−0.9 V vs. RHE for generating CO) [71], and Cu-N_2 (−0.84 V vs. RHE for generating CH_4) [72]. Therefore, the Pd-Nb@In_2Se_3 DAC is a promising candidate for a tunable and efficient eCO_2RR, particularly in achieving high selectivity for final products through controlled polarization modulation.

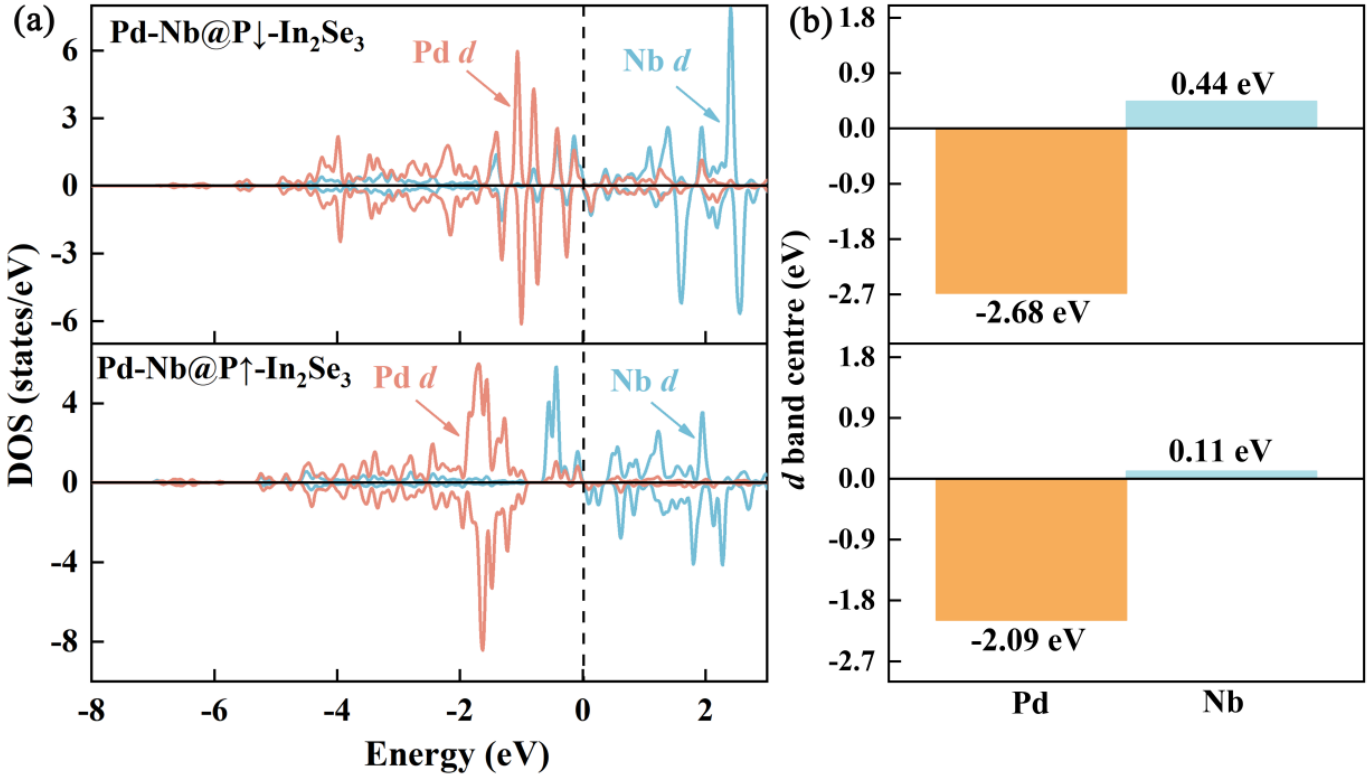

Figure 4. (**a**) Pd *d* orbitals (in light red) from Pd-Nb@P↓-In_2Se_3 and Pd-Nb@P↑-In_2Se_3 DACs. Nb *d* orbitals (in light blue) from Pd-Nb@P↓-In_2Se_3 and Pd-Nb@P↑-In_2Se_3 DACs. (**b**) The *d* band center of Pd-Nb@In_2Se_3, with orange columns for Pd atoms and blue columns for Nb atoms.

2.4. Selectivity for HER vs. eCO_2RR on Pd-Nb@In_2Se_3 DACs

The HER is a prevalent parasitic process in electrochemical systems. It poses a significant challenge to the Faradaic efficiency of the eCO_2RR by diverting critical proton and electron resources from the electrolyte. This competition arises through the HER's multi-step mechanisms—Volmer adsorption, Heyrovsky/Tafel recombination, and H_2 desorption—which operate synergistically to deplete reactive intermediates (H*) and impose additional energy barriers for CO_2 reduction pathways. Particularly in acidic media, the HER's thermodynamic favorability and low activation overpotential exacerbate its dominance over the eCO_2RR, resulting in difficulty in achieving an efficiency of the eCO_2RR that meets the needs of industrial production [73,74]. To check if the eCO_2RR is more favorable, we calculated the Gibbs free energy changes (ΔG) at the first hydrogenation step of the eCO_2RR (* + CO_2 → CO_2*) and the HER (* + H^+ + e^- → H*). As displayed in Figure 6, on the Pd-Nb@P↓-In_2Se_3 DAC, the ΔG for the formation of H* is 0.61 eV, while that of CO_2* is −0.22 eV. As for the case of the Pd-Nb@P↑-In_2Se_3 DAC, the ΔG for the formation of H* is −0.11 eV, while that of CO_2* is −1.04 eV. According to the Brønsted–Evans–Polanyi relation, reactions with lower ΔG have smaller reaction barriers and consequently are kinetically more favorable. The Gibbs free energy changes indicate that the Pd-Nb@In_2Se_3 DACs have a higher selectivity toward the CO_2RR, instead of the HER. These results demonstrate the feasibility of using Pd-Nb@In_2Se_3 catalysts as cathodes for the eCO_2RR with a high Faradaic efficiency.

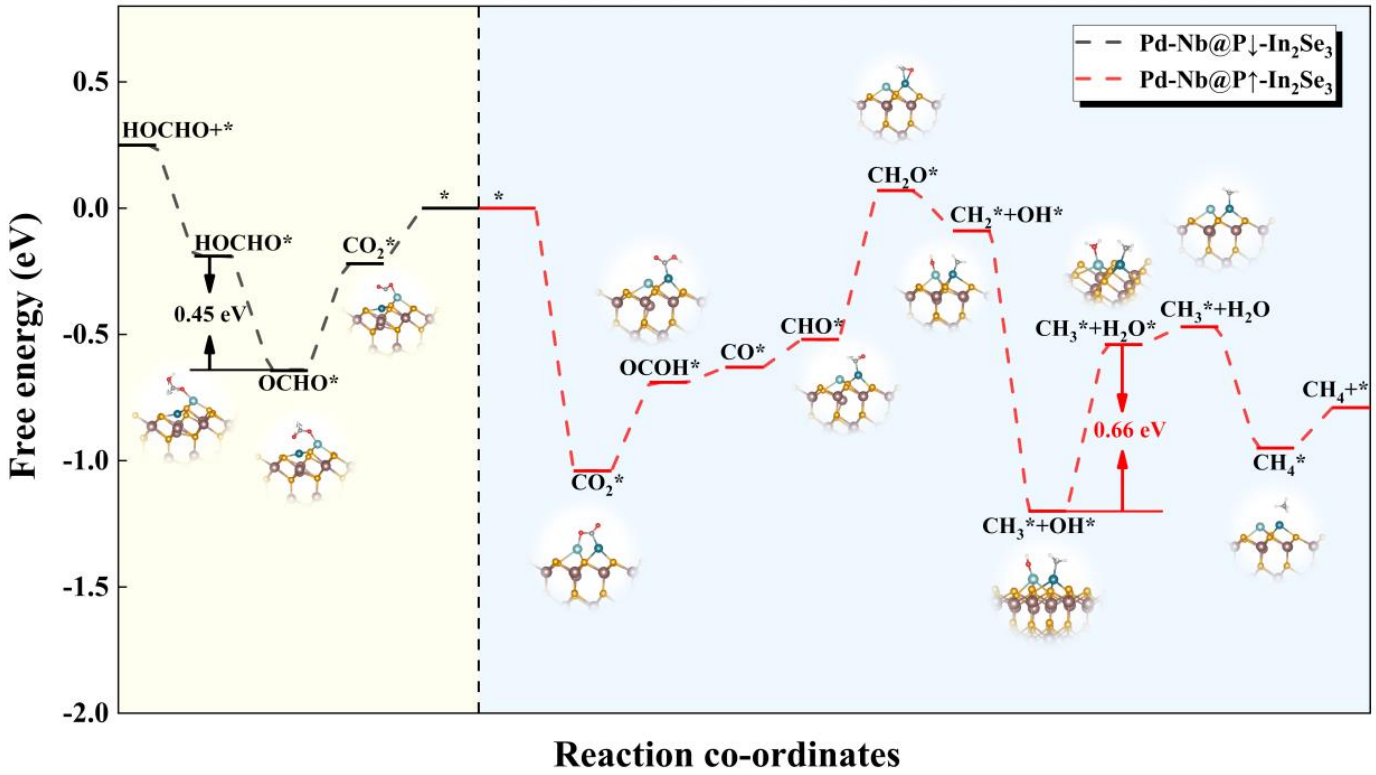

Figure 5. The free-energy profile for the eCO_2RR along the minimum energy path at 0 V (vs. RHE). Energy-minimized structural arrangements of transient species are displayed in the supplementary panels. Gold-shaded region delineates the catalytic process occurring on the Pd-Nb@P↓-In_2Se_3 DAC, while the cyan-tinted zone corresponds to the electrochemical transformation happening on the Pd-Nb@P↑-In_2Se_3 DAC. * stands for the adsorption site at the surface of catalyst.

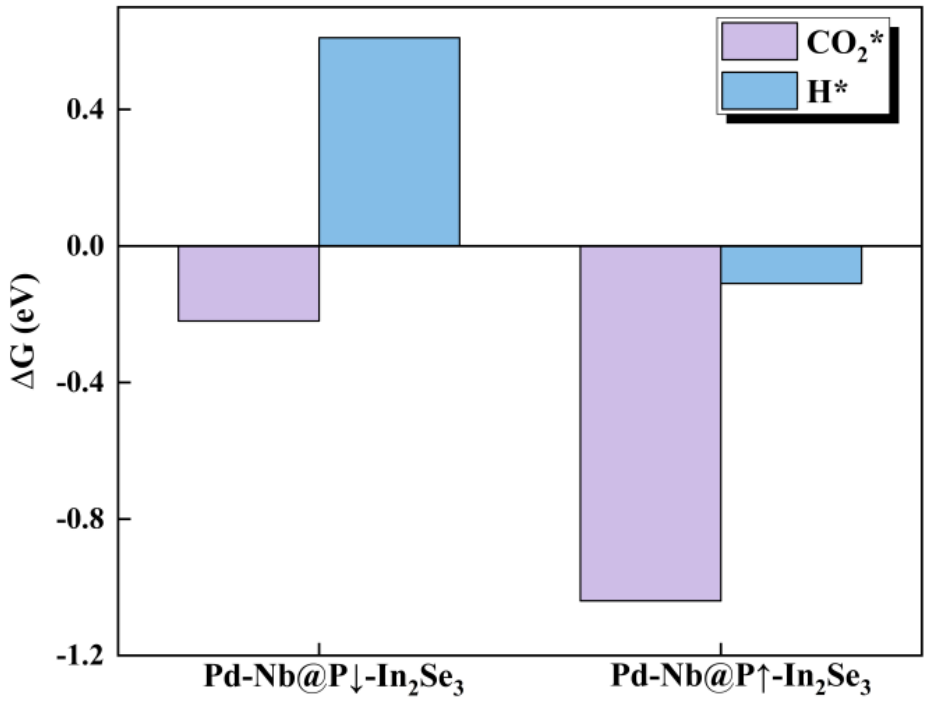

Figure 6. The blue bar indicates the H* formation reaction energy barrier of the optimal active site in the catalyst, and the purple bar indicates the CO_2 adsorption reaction energy barrier. A negative reaction barrier indicates a spontaneous exothermic reaction. * stands for the adsorption site at the surface of catalyst.

3. Methods

All density functional theory (DFT) calculations were performed using the Vienna Ab Initio Simulation Package (VASP) (Hanger team, University of Vienna, version 5.3) [75,76]. The calculations were based on the electron exchange correlation of the PBE generalized function calculation under the generalized gradient approximation (GGA) [77–79]. The van der Waals (vdW) interactions were described by applying Grimme's DFT-D3 method [80], with the colinear spin turned off, the truncation energy set to 500 eV, and the convergence thresholds for force and total energy set to 10^{-2} eV/Å and 10^{-5} eV. The catalytic system was constructed by distributing one Pd atom and one Nb atom on adjacent hexagonal hollow sites of an 4×4 α-In_2Se_3 supercell. For the sampling of the dimensional Brillouin zone, $1 \times 1 \times 1$ gamma-centered Monkhorst-pack k-mesh was chosen for performing structural relaxation and frequency calculations. To minimize periodic image interactions, a vacuum layer exceeding 20 Å was introduced along the non-periodic direction. For Gibbs free energy calculations of the eCO_2RR, solvent effects were accounted for by using the implicit water model in VASPsol (version 5.3) [55,81]. Charge transfer analysis was performed using the Bader charge partitioning method.

The binding energy for the Nb-Pd dual-atom pair ($E_{\text{b-(Nb-Pd)}}$) added onto the substrate was calculated using the following equation [63,82]:

$$E_{\text{b-(Nb-Pd)}} = E_{\text{tot}} - E_{\text{sub}} - E_{\text{Nb}} - E_{\text{Pd}} \quad (1)$$

where E_{sub} and E_{tot} are the total energies of the substrate without and with the added Nb-Pd dual-atom pair, respectively. E_{Nb} and E_{Pd} are the total energy of the isolated Nb and Pd atoms.

The charge density difference ($\Delta\rho$) for the CO_2 molecule adsorbed on Pd-Nb@P↓-In_2Se_3 and Pd-Nb@P↑-In_2Se_3 was calculated using the following equation:

$$\Delta\rho = \rho_{CO_2\text{-}Pd\text{-}Nb\text{-}sub} - \rho_{CO_2} - \rho_{Pd\text{-}Nb\text{-}sub} \quad (2)$$

where $\rho_{CO_2\text{-}Pd\text{-}Nb\text{-}sub}$ and $\rho_{Pd\text{-}Nb\text{-}sub}$ are the charge density of Pd-Nb@In_2Se_3 with and without CO_2 molecules, respectively. ρ_{CO_2} is the charge density of the CO_2 molecule.

In order to obtain the individual orbital components, we employed a code named "splitdos.dos" to process the output file of density of states (DOS). The average *d* band (*d* band center) shifts were calculated for the surface metal atoms for both the total *d* partial DOS and the orbital-resolved *d* partial DOS. The *d* band center (ε_d) was calculated as [83]

$$\varepsilon_d = \frac{\int n_d(\varepsilon)\varepsilon d s}{\int n_d(\varepsilon) d\varepsilon} \quad (3)$$

where ε is the electronic energy of states, and $n_d(\varepsilon)$ is the electronic density of states.

4. Conclusions

Our study presents a theoretical investigation of a novel Pd-Nb@In_2Se_3 DAC for the eCO_2RR, leveraging DFT calculations to elucidate its structural, electronic, and catalytic properties. The Pd-Nb@In_2Se_3 system, anchored on a ferroelectric α-In_2Se_3 monolayer, combines Nb and Pd single atoms to exploit synergistic interactions, while the substrate's switchable polarization enables dynamic control over catalytic activity and selectivity. Structural analyses confirm the stability of Pd-Nb@In_2Se_3, with binding energies of −15.69 eV/unit (P↓ polarization) and −12.27 eV/unit (P↑ polarization) and ab initio molecular dynamics simulations demonstrating thermal stability at 1000 K. The CO_2 adsorption studies revealed enhanced activation on Pd sites, where the linear CO_2 molecule

bends significantly, which is attributed to electron donation/backdonation between CO_2 π orbitals and the Pd/Nb *d* orbitals. The *d* band centers of Pd and Nb atoms, which are closer to the Fermi level in the P↑ configuration, correlate with stronger CO_2 activation, emphasizing the role of electronic structure in catalytic performance. Reaction pathway analyses showed polarization-dependent product selectivity. The P↓ polarization favors formic acid production via a U_l of −0.45 V vs. RHE, while the P↑ polarization directs the reaction toward methane with a U_l of −0.66 V vs. RHE. The dual-site mechanism involves Pd atoms driving carbon reduction and Nb atoms facilitating oxygen removal, synergistically lowering energy barriers compared to their SAC counterparts. Additionally, Gibbs free energy calculations indicate superior selectivity for the CO_2RR over the HER, with CO_2 adsorption energies significantly more favorable than H* formation. The ferroelectric substrate's polarization switching dynamically modulates metal–support interactions, adjusting *d* orbital occupancy and intermediate binding strengths, thereby controlling reaction pathways and product outcomes. This work not only advances the understanding of dual-metal catalysis and polarization–catalysis coupling but also provides a strategy to design tunable electrocatalysts for sustainable energy conversion and CO_2 utilization.

Supplementary Materials: The following supporting information can be downloaded at: https://www.mdpi.com/article/10.3390/inorganics13050146/s1, Table S1: Adsorption energy of CO_2 molecules adsorbed at the adsorption sites of Pd-Nb@In_2Se_3; Table S2: Zero-point energy correction (E_{ZPE}) and entropy contribution (*TS*, T = 298.15 K) of molecules; Table S3: Zero-point energy correction (E_{ZPE}), entropy contribution (*TS*, T = 298.15 K), total energy (*E*), and the Gibbs free energy (*G*) of molecules and adsorbates along the reaction pathway on Pd-Nb@P↓-In_2Se_3, where * represents the adsorption site; Table S4: Zero-point energy correction (E_{ZPE}), entropy contribution (*TS*, *T* = 298.15 K), total energy (*E*), and the Gibbs free energy (*G*) of molecules and adsorbates along the reaction pathway on Pd-Nb@P↑-In_2Se_3, where * represents the adsorption site; Figure S1: Pd *d* orbitals and Nb *d* orbitals from Pd-Nb@In_2Se_3; Figure S2: The selected adsorption sites in Pd-Nb@In_2Se_3; Figure S3: The search process for the minimum energy reaction pathways of the CO_2 reduction reactions on Pd-Nb@In_2Se_3; Figure S4: Three configurations on the optimal CO_2RR reduction path of Pd-Nb@P↑-In_2Se_3; The calculation details of the reaction free energy change. References [84,85] are cited in the supplementary materials.

Author Contributions: Conceptualization, X.T.; data curation, Y.Z.; formal analysis, L.J., X.T., M.C., S.L. and C.L.; funding acquisition, L.J.; investigation, L.J. and X.T.; software, Y.Z.; supervision, L.J.; validation, Y.Z. and M.C.; writing—original draft, L.J., X.T., Y.Z. and S.L. All authors have read and agreed to the published version of the manuscript.

Funding: This study was funded by the Young Scientist Project of Henan Province (Grant No. 225200810103), the Program for Science & Technology Innovation Talents in Universities of Henan Province (Grant No. 24HASTIT013), the College Students Innovation Fund of Anyang Normal University (Grant No. 202410479017), and the Natural Science Foundation of Henan Province (Grant No. 232300420128).

Institutional Review Board Statement: Not applicable.

Informed Consent Statement: Not applicable.

Data Availability Statement: The original contributions presented in this study are included in the article/supplementary material. Further inquiries can be directed to the corresponding author.

Conflicts of Interest: The authors declare no conflict of interest.

References

1. Obama, B. The irreversible momentum of clean energy. *Science* **2017**, *355*, 126–129. [CrossRef] [PubMed]
2. Lüthi, D.; Le Floch, M.; Bereiter, B.; Blunier, T.; Barnola, J.-M.; Siegenthaler, U.; Raynaud, D.; Jouzel, J.; Fischer, H.; Kawamura, K. High-resolution carbon dioxide concentration record 650,000–800,000 years before present. *Nature* **2008**, *453*, 379–382. [CrossRef] [PubMed]
3. Metz, B.; Davidson, O.; De Coninck, H.; Loos, M.; Meyer, L. Intergovernmental panel on climate change. In *IPCC Special Report on Carbon Dioxide Capture and Storage*; Cambridge University Press: New York, NY, USA, 2005; 442p.
4. Chu, S.; Cui, Y.; Liu, N. The path towards sustainable energy. *Nat. Mater.* **2017**, *16*, 16–22. [CrossRef] [PubMed]
5. Yuan, Z.; Zhu, X.; Jiang, Z. Recent Advances of Constructing Metal/Semiconductor Catalysts Designing for Photocatalytic CO_2 Hydrogenation. *Molecules* **2023**, *28*, 5693. [CrossRef]
6. Zhu, X.; Zong, H.; Pérez, C.J.V.; Miao, H.; Sun, W.; Yuan, Z.; Wang, S.; Zeng, G.; Xu, H.; Jiang, Z. Supercharged CO_2 photothermal catalytic methanation: High conversion, rate, and selectivity. *Angew. Chem.* **2023**, *135*, e202218694. [CrossRef]
7. Zhu, X.; Zhou, E.; Tai, X.; Zong, H.; Yi, J.; Yuan, Z.; Zhao, X.; Huang, P.; Xu, H.; Jiang, Z. g-C3N4 S-Scheme Homojunction through Van der Waals Interface Regulation by Intrinsic Polymerization Tailoring for Enhanced Photocatalytic H_2 Evolution and CO_2 Reduction. *Angew. Chem. Int. Ed.* **2025**, *64*, e202425439. [CrossRef]
8. Yap, D.; Megaritis, A. Applying Forced Induction to Bioethanol HCCI Operation with Residual Gas Trapping. *Energy Fuels* **2005**, *19*, 1812–1821. [CrossRef]
9. Kang, Z.; Wu, Z.; Zhang, Z.; Deng, J.; Hu, Z.; Li, L. Study of the Combustion Characteristics of a HCCI Engine Coupled with Oxy-Fuel Combustion Mode. *SAE Int. J. Engines* **2017**, *10*, 908–916. [CrossRef]
10. Berstad, D.; Straus, J.; Gundersen, T. CO_2 capture and enhanced hydrogen production enabled by low-temperature separation of PSA tail gas: A detailed exergy analysis. *Energies* **2024**, *17*, 1072. [CrossRef]
11. Reynolds, S.P.; Ebner, A.D.; Ritter, J.A. Stripping PSA cycles for CO_2 recovery from flue gas at high temperature using a hydrotalcite-like adsorbent. *Ind. Eng. Chem. Res.* **2006**, *45*, 4278–4294. [CrossRef]
12. Hoffert, M.I.; Caldeira, K.; Benford, G.; Criswell, D.R.; Green, C.; Herzog, H.; Jain, A.K.; Kheshgi, H.S.; Lackner, K.S.; Lewis, J.S. Advanced technology paths to global climate stability: Energy for a greenhouse planet. *Science* **2002**, *298*, 981–987. [CrossRef] [PubMed]
13. Duan, X.; Xu, J.; Wei, Z.; Ma, J.; Guo, S.; Wang, S.; Liu, H.; Dou, S. Metal-free carbon materials for CO_2 electrochemical reduction. *Adv. Mater.* **2017**, *29*, 1701784. [CrossRef] [PubMed]
14. Qiao, J.; Liu, Y.; Hong, F.; Zhang, J. A review of catalysts for the electroreduction of carbon dioxide to produce low-carbon fuels. *Chem. Soc. Rev.* **2014**, *43*, 631–675. [CrossRef]
15. Centi, G.; Quadrelli, E.A.; Perathoner, S. Catalysis for CO_2 conversion: A key technology for rapid introduction of renewable energy in the value chain of chemical industries. *Energy Environ. Sci.* **2013**, *6*, 1711–1731. [CrossRef]
16. Ross, M.B.; De Luna, P.; Li, Y.; Dinh, C.-T.; Kim, D.; Yang, P.; Sargent, E.H. Designing materials for electrochemical carbon dioxide recycling. *Nat. Catal.* **2019**, *2*, 648–658. [CrossRef]
17. Wang, G.; Zhong, S.; Xiong, X.; Li, J.; Wang, F.; Huo, L.; Wu, D.; Han, X.; Wang, Z.; Chen, Q. Plasma induced grain boundaries to boost electrochemical reduction of CO_2 to formate. *J. Energy Chem.* **2024**, *95*, 636–643. [CrossRef]
18. Wei, Z.; Wang, W.; Shao, T.; Yang, S.; Liu, C.; Si, D.; Cao, R.; Cao, M. Constructing Ag/Cu_2O interface for efficient neutral CO_2 electroreduction to C_2H_4. *Angew. Chem. Int. Ed.* **2025**, *64*, e202417066. [CrossRef]
19. Yue, M.; Xie, W.; Zhong, Z.; Li, M.; Zhang, T.; Shao, M.; Li, H.; Wang, Q. Isolating and stabilizing active copper species in layered double hydroxide to enhance electrocatalytic CO_2 reduction to CH_4. *J. Catal.* **2025**, *443*, 115959. [CrossRef]
20. Dong, J.; Liu, Y.; Pei, J.; Li, H.; Ji, S.; Shi, L.; Zhang, Y.; Li, C.; Tang, C.; Liao, J. Continuous electroproduction of formate via CO_2 reduction on local symmetry-broken single-atom catalysts. *Nat. Commun.* **2023**, *14*, 6849. [CrossRef]
21. Chatterjee, S.; Dutta, I.; Lum, Y.; Lai, Z.; Huang, K.-W. Enabling storage and utilization of low-carbon electricity: Power to formic acid. *Energy Environ. Sci.* **2021**, *14*, 1194–1246. [CrossRef]
22. Li, M.; Idros, M.N.; Wu, Y.; Burdyny, T.; Garg, S.; Zhao, X.S.; Wang, G.; Rufford, T.E. The role of electrode wettability in electrochemical reduction of carbon dioxide. *J. Mater. Chem. A* **2021**, *9*, 19369–19409. [CrossRef]
23. Möller, T.; Ju, W.; Bagger, A.; Wang, X.; Luo, F.; Ngo Thanh, T.; Varela, A.S.; Rossmeisl, J.; Strasser, P. Efficient CO_2 to CO electrolysis on solid Ni–N–C catalysts at industrial current densities. *Energy Environ. Sci.* **2019**, *12*, 640–647. [CrossRef]
24. Guo, S.; Liu, Y.; Murphy, E.; Ly, A.; Xu, M.; Matanovic, I.; Pan, X.; Atanassov, P. Robust palladium hydride catalyst for electrocatalytic formate formation with high CO tolerance. *Appl. Catal. B Environ.* **2022**, *316*, 121659. [CrossRef]
25. Detweiler, Z.M.; White, J.L.; Bernasek, S.L.; Bocarsly, A.B. Anodized indium metal electrodes for enhanced carbon dioxide reduction in aqueous electrolyte. *Langmuir* **2014**, *30*, 7593–7600. [CrossRef]
26. Ikeda, S.; Takagi, T.; Ito, K. Selective formation of formic acid, oxalic acid, and carbon monoxide by electrochemical reduction of carbon dioxide. *Bull. Chem. Soc. Jpn.* **1987**, *60*, 2517–2522. [CrossRef]

27. Hori, Y.; Wakebe, H.; Tsukamoto, T.; Koga, O. Electrocatalytic process of CO selectivity in electrochemical reduction of CO_2 at metal electrodes in aqueous media. *Electrochim. Acta* **1994**, *39*, 1833–1839. [CrossRef]
28. Ding, S.; Hülsey, M.J.; Pérez-Ramírez, J.; Yan, N. Transforming energy with single-atom catalysts. *Joule* **2019**, *3*, 2897–2929. [CrossRef]
29. Su, X.; Yang, X.-F.; Huang, Y.; Liu, B.; Zhang, T. Single-atom catalysis toward efficient CO_2 conversion to CO and formate products. *Acc. Chem. Res.* **2018**, *52*, 656–664. [CrossRef]
30. Liu, K.; Fu, J.; Zhu, L.; Zhang, X.; Li, H.; Liu, H.; Hu, J.; Liu, M. Single-atom transition metals supported on black phosphorene for electrochemical nitrogen reduction. *Nanoscale* **2020**, *12*, 4903–4908. [CrossRef]
31. Lu, F.; Yi, D.; Liu, S.; Zhan, F.; Zhou, B.; Gu, L.; Golberg, D.; Wang, X.; Yao, J. Engineering platinum–oxygen dual catalytic sites via charge transfer towards highly efficient hydrogen evolution. *Angew. Chem.* **2020**, *132*, 17865–17871. [CrossRef]
32. Nguyen, T.; Salehi, M.; Le, Q.; Seifitokaldani, A.; Dinh, C. Fundamentals of electrochemical CO_2 reduction on single-metal-atom catalysts. *ACS Catal.* **2020**, *10*, 10068–10095. [CrossRef]
33. Sun, J.-F.; Wu, J.-T.; Xu, Q.-Q.; Zhou, D.; Yin, J.-Z. CO_2 electrochemical reduction using single-atom catalysts. Preparation, characterization and anchoring strategies: A review. *Environ. Chem. Lett.* **2020**, *18*, 1593–1623. [CrossRef]
34. Asset, T.; Garcia, S.T.; Herrera, S.; Andersen, N.; Chen, Y.; Peterson, E.J.; Matanovic, I.; Artyushkova, K.; Lee, J.; Minteer, S.D. Investigating the nature of the active sites for the CO2 reduction reaction on carbon-based electrocatalysts. *ACS Catal.* **2019**, *9*, 7668–7678. [CrossRef]
35. Zhang, Q.; Guan, J. Single-atom catalysts for electrocatalytic applications. *Adv. Funct. Mater.* **2020**, *30*, 2000768. [CrossRef]
36. Zhang, Y.; Xia, B.; Ran, J.; Davey, K.; Qiao, S.Z. Atomic-level reactive sites for semiconductor-based photocatalytic CO_2 reduction. *Adv. Energy Mater.* **2020**, *10*, 1903879. [CrossRef]
37. Luo, G.; Jing, Y.; Li, Y. Rational design of dual-metal-site catalysts for electroreduction of carbon dioxide. *J. Mater. Chem. A* **2020**, *8*, 15809–15815. [CrossRef]
38. Ouyang, Y.; Shi, L.; Bai, X.; Li, Q.; Wang, J. Breaking scaling relations for efficient CO_2 electrochemical reduction through dual-atom catalysts. *Chem. Sci.* **2020**, *11*, 1807–1813. [CrossRef]
39. Li, Y.; Chen, C.; Cao, R.; Pan, Z.; He, H.; Zhou, K. Dual-atom Ag_2/graphene catalyst for efficient electroreduction of CO_2 to CO. *Appl. Catal. B Environ.* **2020**, *268*, 118747. [CrossRef]
40. Li, Y.; Su, H.; Chan, S.H.; Sun, Q. CO_2 Electroreduction Performance of Transition Metal Dimers Supported on Graphene: A Theoretical Study. *ACS Catal.* **2015**, *5*, 6658–6664. [CrossRef]
41. Li, X.; Sun, Y.; Xu, J.; Shao, Y.; Wu, J.; Xu, X.; Pan, Y.; Ju, H.; Zhu, J.; Xie, Y. Selective visible-light-driven photocatalytic CO_2 reduction to CH_4 mediated by atomically thin $CuIn_5S_8$ layers. *Nat. Energy* **2019**, *4*, 690–699. [CrossRef]
42. Li, S.; Nagarajan, A.V.; Alfonso, D.R.; Sun, M.; Kauffman, D.R.; Mpourmpakis, G.; Jin, R. Boosting CO_2 electrochemical reduction with atomically precise surface modification on gold nanoclusters. *Angew. Chem. Int. Ed.* **2021**, *60*, 6351–6356. [CrossRef] [PubMed]
43. Wen, G.; Lee, D.U.; Ren, B.; Hassan, F.M.; Jiang, G.; Cano, Z.P.; Gostick, J.; Croiset, E.; Bai, Z.; Yang, L. Orbital interactions in Bi-Sn bimetallic electrocatalysts for highly selective electrochemical CO_2 reduction toward formate production. *Adv. Energy Mater.* **2018**, *8*, 1802427. [CrossRef]
44. Lin, L.; Li, H.; Yan, C.; Li, H.; Si, R.; Li, M.; Xiao, J.; Wang, G.; Bao, X. Synergistic catalysis over iron-nitrogen sites anchored with cobalt phthalocyanine for efficient CO_2 electroreduction. *Adv. Mater.* **2019**, *31*, 1903470. [CrossRef]
45. Hu, K.; Li, Z.; Bai, L.; Yang, F.; Chu, X.; Bian, J.; Zhang, Z.; Xu, H.; Jing, L. Synergetic subnano Ni-and Mn-Oxo clusters anchored by chitosan oligomers on 2D g-C_3N_4 boost photocatalytic CO_2 reduction. *Sol. Rrl* **2021**, *5*, 2000472. [CrossRef]
46. Bok, J.; Lee, S.Y.; Lee, B.-H.; Kim, C.; Nguyen, D.L.T.; Kim, J.W.; Jung, E.; Lee, C.W.; Jung, Y.; Lee, H.S. Designing atomically dispersed Au on tensile-strained Pd for efficient CO_2 electroreduction to formate. *J. Am. Chem. Soc.* **2021**, *143*, 5386–5395. [CrossRef]
47. Ding, T.; Liu, X.; Tao, Z.; Liu, T.; Chen, T.; Zhang, W.; Shen, X.; Liu, D.; Wang, S.; Pang, B. Atomically precise dinuclear site active toward electrocatalytic CO_2 reduction. *J. Am. Chem. Soc.* **2021**, *143*, 11317–11324. [CrossRef]
48. He, Q.; Liu, D.; Lee, J.H.; Liu, Y.; Xie, Z.; Hwang, S.; Kattel, S.; Song, L.; Chen, J.G. Electrochemical conversion of CO_2 to syngas with controllable CO/H_2 ratios over Co and Ni single-atom catalysts. *Angew. Chem. Int. Ed.* **2020**, *59*, 3033–3037. [CrossRef]
49. Darif, B.; Ojala, S.; Pirault-Roy, L.; Bensitel, M.; Brahmi, R.; Keiski, R.L. Study on the catalytic oxidation of DMDS over Pt-Cu catalysts supported on Al_2O_3, $AlSi_{20}$ and SiO_2. *Appl. Catal. B Environ.* **2016**, *181*, 24–33. [CrossRef]
50. Winter, L.R.; Gomez, E.; Yan, B.; Yao, S.; Chen, J.G. Tuning Ni-catalyzed CO_2 hydrogenation selectivity via Ni-ceria support interactions and Ni-Fe bimetallic formation. *Appl. Catal. B Environ.* **2018**, *224*, 442–450. [CrossRef]
51. Wang, J.; Huang, Z.; Liu, W.; Chang, C.; Tang, H.; Li, Z.; Chen, W.; Jia, C.; Yao, T.; Wei, S.; et al. Design of N-Coordinated Dual-Metal Sites: A Stable and Active Pt-Free Catalyst for Acidic Oxygen Reduction Reaction. *J. Am. Chem. Soc.* **2017**, *139*, 17281–17284. [CrossRef]
52. Ren, W.; Tan, X.; Yang, W.; Jia, C.; Xu, S.; Wang, K.; Smith, S.C.; Zhao, C. Isolated Diatomic Ni-Fe Metal–Nitrogen Sites for Synergistic Electroreduction of CO_2. *Angew. Chem. Int. Ed.* **2019**, *58*, 6972–6976. [CrossRef] [PubMed]

53. Zhang, L.; Fischer, J.M.T.A.; Jia, Y.; Yan, X.; Xu, W.; Wang, X.; Chen, J.; Yang, D.; Liu, H.; Zhuang, L.; et al. Coordination of Atomic Co–Pt Coupling Species at Carbon Defects as Active Sites for Oxygen Reduction Reaction. *J. Am. Chem. Soc.* **2018**, *140*, 10757–10763. [CrossRef] [PubMed]
54. Li, D.; Zhao, M.H.; Garra, J.; Kolpak, A.M.; Rappe, A.M.; Bonnell, D.A.; Vohs, J.M. Direct in situ determination of the polarization dependence of physisorption on ferroelectric surfaces. *Nat. Mater.* **2008**, *7*, 473–477. [CrossRef]
55. Ju, L.; Shang, J.; Tang, X.; Kou, L. Tunable Photocatalytic Water Splitting by the Ferroelectric Switch in a 2D $AgBiP_2Se_6$ Monolayer. *J. Am. Chem. Soc.* **2019**, *142*, 1492–1500. [CrossRef]
56. Ju, L.; Tan, X.; Mao, X.; Gu, Y.; Smith, S.; Du, A.; Chen, Z.; Chen, C.; Kou, L. Controllable CO_2 electrocatalytic reduction via ferroelectric switching on single atom anchored In_2Se_3 monolayer. *Nat. Commun.* **2021**, *12*, 5128. [CrossRef]
57. Ding, W.; Zhu, J.; Wang, Z.; Gao, Y.; Xiao, D.; Gu, Y.; Zhang, Z.; Zhu, W. Prediction of intrinsic two-dimensional ferroelectrics in In_2Se_3 and other III_2-VI_3 van der Waals materials. *Nat. Commun.* **2017**, *8*, 14956. [CrossRef]
58. Cui, C.; Hu, W.J.; Yan, X.; Addiego, C.; Gao, W.; Wang, Y.; Wang, Z.; Li, L.; Cheng, Y.; Li, P.; et al. Intercorrelated In-Plane and Out-of-Plane Ferroelectricity in Ultrathin Two-Dimensional Layered Semiconductor In_2Se_3. *Nano Lett.* **2018**, *18*, 1253–1258. [CrossRef]
59. Gao, G.; Jiao, Y.; Waclawik, E.R.; Du, A. Single Atom (Pd/Pt) Supported on Graphitic Carbon Nitride as an Efficient Photocatalyst for Visible-Light Reduction of Carbon Dioxide. *J. Am. Chem. Soc.* **2016**, *138*, 6292–6297. [CrossRef]
60. Li, X.; Bi, W.; Zhang, L.; Tao, S.; Chu, W.; Zhang, Q.; Luo, Y.; Wu, C.; Xie, Y. Single-Atom Pt as Co-Catalyst for Enhanced Photocatalytic H_2 Evolution. *Adv. Mater.* **2016**, *28*, 2427–2431. [CrossRef]
61. Vile, G.; Albani, D.; Nachtegaal, M.; Chen, Z.; Dontsova, D.; Antonietti, M.; Lopez, N.; Perez-Ramirez, J. A stable single-site palladium catalyst for hydrogenations. *Angew. Chem. Int. Ed.* **2015**, *54*, 11265–11269. [CrossRef]
62. Khatun, R.; Siddiqui, N.; Pal, R.S.; Bhandari, S.; Khan, T.S.; Singh, S.; Poddar, M.K.; Samanta, C.; Bal, R. Low temperature reforming of methane with CO_2 over Pt/CeO_2, Ni/CeO_2 and $Pt–Ni/CeO_2$ catalysts prepared by a solution-combustion method. *Catal. Sci. Technol.* **2023**, *13*, 6431–6445. [CrossRef]
63. Ma, D.; Zeng, Z.; Liu, L.; Huang, X.; Jia, Y. Computational Evaluation of Electrocatalytic Nitrogen Reduction on TM Single-, Double-, and Triple-Atom Catalysts (TM = Mn, Fe, Co, Ni) Based on Graphdiyne Monolayers. *J. Phys. Chem. C* **2019**, *123*, 19066–19076. [CrossRef]
64. Back, S.; Kim, H.; Jung, Y. Selective Heterogeneous CO_2 Electroreduction to Methanol. *ACS Catal.* **2015**, *5*, 965–971. [CrossRef]
65. Zhao, Z.; Lu, G. Cu-Based Single-Atom Catalysts Boost Electroreduction of CO_2 to CH_3OH: First-Principles Predictions. *J. Phys. Chem. C* **2019**, *123*, 4380–4387. [CrossRef]
66. Wannakao, S.; Artrith, N.; Limtrakul, J.; Kolpak, A.M. Engineering Transition-Metal-Coated Tungsten Carbides for Efficient and Selective Electrochemical Reduction of CO_2 to Methane. *ChemSusChem* **2015**, *8*, 2745–2751. [CrossRef]
67. Elhenawy, S.E.M.; Khraisheh, M.; AlMomani, F.; Walker, G. Metal-organic frameworks as a platform for CO_2 capture and chemical processes: Adsorption, membrane separation, catalytic-conversion, and electrochemical reduction of CO_2. *Catalysts* **2020**, *10*, 1293. [CrossRef]
68. Zhang, N.; Zhang, X.; Kang, Y.; Ye, C.; Jin, R.; Yan, H.; Lin, R.; Yang, J.; Xu, Q.; Wang, Y.; et al. A Supported Pd_2 Dual-Atom Site Catalyst for Efficient Electrochemical CO_2 Reduction. *Angew. Chem. Int. Ed.* **2021**, *60*, 13388–13393. [CrossRef]
69. Hao, Q.; Zhong, H.; Wang, J.; Liu, K.; Yan, J.; Ren, Z.; Zhou, N.; Zhao, X.; Zhang, H.; Liu, D.; et al. Nickel dual-atom sites for electrochemical carbon dioxide reduction. *Nat. Synth.* **2022**, *1*, 719–728. [CrossRef]
70. Huang, K.; Li, R.; Qi, H.; Yang, S.; An, S.; Lian, C.; Xu, Q.; Liu, H.; Hu, J. Regulating Adsorption of Intermediates via the Sulfur Modulating Dual-Atomic Sites for Boosting CO_2RR. *ACS Catal.* **2024**, *14*, 8889–8898. [CrossRef]
71. Chen, B.; Shi, D.; Deng, R.; Xu, X.; Liu, W.; Wei, Y.; Liu, Z.; Zhong, S.; Huang, J.; Yu, Y. Leveraging Atomic-Scale Synergy for Selective CO_2 Electrocatalysis to CO over CuNi Dual-Atom Catalysts. *ACS Catal.* **2024**, *14*, 16224–16233. [CrossRef]
72. Roy, S.; Li, Z.; Chen, Z.; Mata, A.C.; Kumar, P.; Sarma, S.C.; Teixeira, I.F.; Silva, I.F.; Gao, G.; Tarakina, N.V.; et al. Cooperative Copper Single-Atom Catalyst in 2D Carbon Nitride for Enhanced CO_2 Electrolysis to Methane. *Adv. Mater.* **2024**, *36*, e2300713. [CrossRef]
73. Xue, H.; Zhao, Z.H.; Liao, P.Q.; Chen, X.M. "Ship-in-a-Bottle" Integration of Ditin(IV) Sites into a Metal-Organic Framework for Boosting Electroreduction of CO_2 in Acidic Electrolyte. *J. Am. Chem. Soc.* **2023**, *145*, 16978–16982. [CrossRef]
74. Monteiro, M.C.O.; Dattila, F.; Hagedoorn, B.; García-Muelas, R.; López, N.; Koper, M.T.M. Absence of CO_2 electroreduction on copper, gold and silver electrodes without metal cations in solution. *Nat. Catal.* **2021**, *4*, 654–662. [CrossRef]
75. Kresse, G.; Furthmüller, J. Efficient iterative schemes for ab initio total-energy calculations using a plane-wave basis set. *Phys. Rev. B* **1996**, *54*, 11169. [CrossRef]
76. Kresse, G.; Furthmüller, J. Efficiency of ab-initio total energy calculations for metals and semiconductors using a plane-wave basis set. *Comput. Mater. Sci.* **1996**, *6*, 15–50. [CrossRef]
77. Blöchl, P.E. Projector augmented-wave method. *Phys. Rev. B* **1994**, *50*, 17953–17979. [CrossRef]
78. Kresse, G.; Joubert, D. From ultrasoft pseudopotentials to the projector augmented-wave method. *Phys. Rev. B* **1999**, *59*, 1758. [CrossRef]

79. Perdew, J.P.; Burke, K.; Ernzerhof, M. Generalized gradient approximation made simple. *Phys. Rev. Lett.* **1996**, *77*, 3865. [CrossRef]
80. Grimme, S. Semiempirical GGA-type density functional constructed with a long-range dispersion correction. *J. Comput. Chem.* **2006**, *27*, 1787–1799. [CrossRef]
81. Mao, X.; Kour, G.; Zhang, L.; He, T.; Wang, S.; Yan, C.; Zhu, Z.; Du, A. Silicon-doped graphene edges: An efficient metal-free catalyst for the reduction of CO_2 into methanol and ethanol. *Catal. Sci. Technol.* **2019**, *9*, 6800–6807. [CrossRef]
82. Cui, X.; An, W.; Liu, X.; Wang, H.; Men, Y.; Wang, J. C_2N-graphene supported single-atom catalysts for CO_2 electrochemical reduction reaction: Mechanistic insight and catalyst screening. *Nanoscale* **2018**, *10*, 15262–15272. [CrossRef] [PubMed]
83. Nørskov, J.K.; Studt, F.; Abild-Pedersen, F.; Bligaard, T. Fundamental Concepts in Heterogeneous Catalysis. *Focus Catal.* **2015**, *2015*, 7. [CrossRef]
84. Nørskov, J.K.; Rossmeisl, J.; Logadottir, A.; Lindqvist, L.; Kitchin, J.R.; Bligaard, T.; Jonsson, H. Origin of the overpotential for oxygen reduction at a fuel-cell cathode. *J. Phys. Chem. B* **2004**, *108*, 17886–17892. [CrossRef]
85. Peterson, A.A.; Abild-Pedersen, F.; Studt, F.; Rossmeisl, J.; Nørskov, J.K. How copper catalyzes the electroreduction of carbon dioxide into hydrocarbon fuels. *Energ. Environ. Sci.* **2010**, *3*, 1311–1315. [CrossRef]

Disclaimer/Publisher's Note: The statements, opinions and data contained in all publications are solely those of the individual author(s) and contributor(s) and not of MDPI and/or the editor(s). MDPI and/or the editor(s) disclaim responsibility for any injury to people or property resulting from any ideas, methods, instructions or products referred to in the content.